

**Dynamical Measurement of Supermassive Black Hole Masses: QPE Timing Method**CONG ZHOU <sup>1,2</sup> ZHEN PAN <sup>3,4</sup> AND NING JIANG <sup>1,2</sup><sup>1</sup>*Department of Astronomy, University of Science and Technology of China, Hefei 230026, People's Republic of China*<sup>2</sup>*School of Astronomy and Space Sciences, University of Science and Technology of China, Hefei 230026, People's Republic of China*<sup>3</sup>*Tsung-Dao Lee Institute, Shanghai Jiao-Tong University, Shanghai, 520 Shengrong Road, 201210, People's Republic of China*<sup>4</sup>*School of Physics & Astronomy, Shanghai Jiao-Tong University, Shanghai, 800 Dongchuan Road, 200240, People's Republic of China***ABSTRACT**

Quasi-periodic eruptions (QPEs) are intense repeating soft X-ray bursts with recurrence times about a few hours to a few weeks from galactic nuclei. More and more analyses show that (at least a fraction of) QPEs are the result of collisions between a stellar mass object (SMO, a stellar mass black hole or a main sequence star) and an accretion disk around a supermassive black hole (SMBH) in galactic nuclei. Previous studies have shown that the SMO trajectory can be reconstructed from QPE timing data, consequently the SMBH mass can be robustly measured from tracing a single SMO. In this Letter, we construct a comprehensive Bayesian framework for implementing the QPE timing method, explore the optimal QPE observation strategy for measuring SMBH masses, and forecast the measurement precision expected in the era of multi-target X-ray telescope, Chasing All Transients Constellation Hunters (CATCH). As a result, we find the QPE timing method is of great potential in precise measurement of SMBH masses (and spins), especially in the lower mass end ( $\lesssim 10^7 M_\odot$ ) where QPEs prevail and relevant dynamical timescales are reasonably short to be measured.

**Keywords:** Supermassive black holes (1663), Tidal disruption (1696), Active galactic nuclei (16), General relativity (641), Apsidal motion (62), Keplerian orbit (884)

**1. INTRODUCTION**

It is nowadays widely accepted that supermassive black holes (SMBHs) with masses ranging from  $\sim 10^5 - 10^{10} M_\odot$  reside at the centers of most, if not all, massive galaxies with substantial spheroidal (bulge) components, both quiescent and active (see reviews by [Kormendy & Richstone 1995](#); [Kormendy & Ho 2013](#)). However, a precise measurement of the masses of SMBHs ( $M_\bullet$ ) has been a challenge since it is of great difficulty to directly probe the motion of objects in the vicinity of SMBHs, where the gravitational potential of the SMBHs exerts a dominant influence. In fact, aside from Sagittarius A\* at the center of our Milky Way ([Schödel et al. 2002](#); [Ghez et al. 2005](#); [Gillessen et al. 2009](#); [GRAVITY Collaboration et al. 2018](#)), we have not been able to effectively

resolve individual stars or gas clouds around SMBHs. Instead, we can only measure the collective motion of stars or gas within a given region as a whole even taking advantage of highly spatially resolved observations of Hubble Space Telescope (HST) and large adaptive optics (AO)-assisted ground-based telescopes. Therefore, the  $M_\bullet$  measurement suffers from additional uncertainties from velocity smoothing and galaxy central mass distribution in the dynamical modeling. So far, only a total of hundreds of SMBHs in the local galaxies ( $\lesssim 100$  Mpc) have been weighted by the so-called stellar and gas kinematics. Moreover, these SMBHs are found to be correlated with the bulge properties of their host galaxies, most commonly known as the  $M_\bullet$ - $\sigma_\star$  relation in which the  $\sigma_\star$  refers to the stellar velocity dispersion ([Ferrarese & Merritt 2000](#); [Gebhardt et al. 2000](#)), making the field of BH-galaxy co-evolution a frontier of astronomy over the past two decades (see reviews by [Kormendy & Ho 2013](#); [Heckman & Best 2014](#)). These correlations themselves offer a new and more convenient approach to estimate the  $M_\bullet$  since the kinematic method used in local massive galaxies cannot be extended to more distant or dwarf galaxies.

dysania@mail.ustc.edu.cn

zhpan@sjtu.edu.cn

jnac@ustc.edu.cn

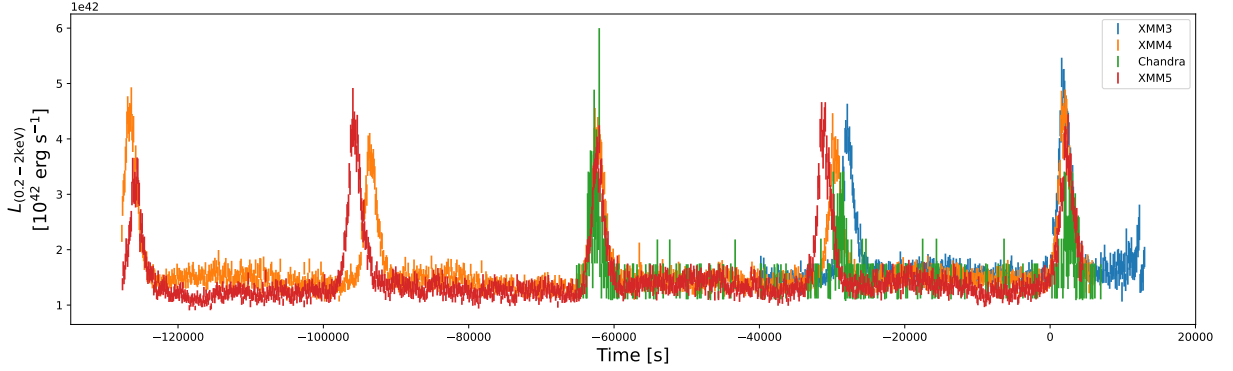


**Figure 1.** GSN 069 QPE light curves from 4 observations during Dec. 2018-May 2019 (Miniutti et al. 2019, 2023b), where the recurrence times show an alternating long-short pattern  $T_{\text{long,short}}$ , with both  $T_{\text{long}}$  and  $T_{\text{short}}$  showing clear variations while the sum of two consecutive recurrence times  $T_{\text{long}} + T_{\text{short}}$  remains approximately a constant (Zhou et al. 2024).

Although the  $M_{\bullet} - \sigma_{\star}$  and the  $M_{\bullet} - M_{\star}$  relations have been widely used to infer  $M_{\bullet}$  when the host bulge mass  $M_{\star}$  or the stellar velocity dispersion  $\sigma_{\star}$  is available, it is important to recognize their uncertainties, i.e. 0.3 – 0.4 dex intrinsic scatter even when only considering elliptical galaxies and classical bulges (Gültekin et al. 2009; Kormendy & Ho 2013; McConnell & Ma 2013). Furthermore, these relations are primarily established based on SMBHs with  $M_{\bullet} \gtrsim 10^7 M_{\odot}$ , leading to larger uncertainties for lower mass black holes, i.e.  $M_{\bullet} \lesssim 10^6 M_{\odot}$ , either due to a larger intrinsic scatter or a possible systematic error.

For active galactic nuclei (AGNs), perhaps the most popular method of measuring  $M_{\bullet}$  is the virial mass, which assumes that the broad-line region (BLR) is virialized and the motions of clouds are governed by the gravity of SMBH (see reviews by Shen 2013; Peterson 2014). There is a vague coefficient  $f$  in the calculation whose average value is calibrated by the  $M_{\bullet} - \sigma_{\star}$  relation. It means, in principle, that the virial mass estimator can not be more accurate than  $M_{\bullet} - \sigma_{\star}$  relation. Moreover,  $f$  is likely to vary from object to object, since it depends on the kinematics, geometry, inclination of the clouds, and even the types of the bulges (Ho & Kim 2014). Recently, the evolutionary NIR interferometry GRAVITY, mounted on the Very Large Telescope Interferometer (VLTI), has opened up a new era of probing the BLR structure and has great potential to improve the precision of the  $M_{\bullet}$  measurement (Gravity Collaboration et al. 2018; Abuter et al. 2024), but it can only apply to very few K-band luminous AGNs.

In this Letter, we propose a novel method to measure the  $M_{\bullet}$  with unprecedented precision using the quasi-periodic eruption (QPE) phenomenon. QPEs are intense repeating soft X-ray bursts with recurrence times about a few hours to a few weeks from galactic nuclei nearby. Starting from the first detection more than a decade ago (Sun et al. 2013), QPEs from about ten different nearby galactic nuclei have been re-

ported (Miniutti et al. 2019; Giustini et al. 2020; Arcodia et al. 2021, 2022; Chakraborty et al. 2021; Evans et al. 2023; Guolo et al. 2024; Arcodia et al. 2024; Nicholl et al. 2024; Chakraborty et al. 2025; Hernández-García et al. 2025). The QPEs are detected in the soft X-ray band with similar peak luminosities ( $10^{42} - 10^{43}$  ergs  $s^{-1}$ ), thermal-like X-ray spectra with temperature  $kT \simeq 100 - 250$  eV and the temperature 50 – 80 eV in the quiescent state.

Though there have been some debates on the origin of QPEs, more and more analyses favor the extreme mass ratio inspiral (EMRI) + accretion disk model, where the QPEs are the result of collisions between a stellar mass object (SMO, a stellar mass black hole or a main sequence star) and an accretion disk around a SMBH in galactic nuclei (see e.g., Xian et al. 2021; Franchini et al. 2023; Tagawa & Haiman 2023; Arcodia et al. 2024; Guolo et al. 2024; Zhou et al. 2024; Zhou et al. 2024b,a; Linial & Quataert 2023; Linial & Metzger 2023a,b; Chakraborty et al. 2024; Linial & Metzger 2024; Arcodia et al. 2024a; Yao et al. 2024; Giustini et al. 2024; Vurm et al. 2024; Pasham et al. 2024; Pasham et al. 2024; Miniutti et al. 2024 for details). Among all the observations, two pieces of direct observational evidence for the EMRI+disk model have been recognized. Recently, QPEs in X-ray light curves of three tidal disruption events (TDEs)  $O(1)$  years after their ignitions have been directly detected (Nicholl et al. 2024; Bykov et al. 2024; Chakraborty et al. 2025). Moreover, the QPE hosts and TDE hosts show strikingly morphological similarities (Gilbert et al. 2024) and a preference for extending emission line regions indicative of recently faded AGNs (Wevers et al. 2024). The other observational evidence is about the alternating long-short pattern in the QPE recurrence times which has long been noticed in several QPE sources (Miniutti et al. 2019; Giustini et al. 2020; Arcodia et al. 2021, 2022), including the most famous source GSN 069. A more intriguing feature in the QPE timing was identified by Zhou et al. (2024): there are large vari-

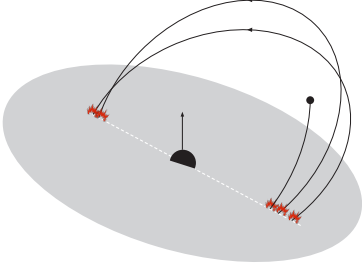


**Figure 2.** Schematic picture of the EMRI+disk model, where the EMRI collides the disk at a different location each time due to apsidal precession, and the EMRI orbital plane precesses on an even longer Lense-Thirring precession timescale if the central SMBH is spinning.

ations in both the long and the short recurrence times of GSN 069 QPEs  $T_{\text{long,short}}(t)$ , while  $T_{\text{long}}(t) + T_{\text{short}}(t)$  remains nearly a constant (see Fig. 1). This observation strongly implies that  $T_{\text{long}} + T_{\text{short}}$  is the fundamental period of underlying physical process that is sourcing the QPEs, and two flares with varying intervals are produced per fundamental period. These two observations naturally fit in the EMRI+disk model (see Fig. 2), while are hardly explained by other models in a natural way. Therefore, a unified model proposes that both TDEs and QPEs are the embers of AGNs, where AGNs increase both the TDE rate and the formation rate of low eccentricity EMRIs, and QPEs are preferentially found in recently faded AGNs, where TDEs often feed a misaligned accretion disk to the EMRI (Jiang & Pan 2025).

In the framework of EMRI+disk model, a range of astrophysical applications of QPEs have been investigated, including measuring SMBH parameters, probing structure of SMBH accretion disks, formation processes and formation rates of EMRIs (Xian et al. 2021; Zhou et al. 2024; Zhou et al. 2024b,a; Arcodia et al. 2024b; Kaur et al. 2024) and implications for potential multi-messenger observations of EMRIs in the era of spaceborne gravitational wave astrophysics (Kejriwal et al. 2024). In this work, we will focus on measuring SMBH masses with QPE timing data, which we have briefly discussed in previous works (Zhou et al. 2024; Zhou et al. 2024b,a) (hereafter papers I-III). Using the QPE timing method, one can reconstruct the trajectory of a single SMO around a SMBH, therefore accurately measure the orbital parameters and the SMBH mass.

The QPE timing method is a truly direct dynamic measurement achieved by tracing the motion of a single star orbiting around a SMBH, thereby circumventing many uncertainties

related to both measurement and systematic errors involved in traditional methods. This method is in the same spirit of measuring the Sagittarius A\* SMBH mass by monitoring orbits of individual stars (Schödel et al. 2002; Ghez et al. 2005; Gillessen et al. 2009; GRAVITY Collaboration et al. 2018). As QPEs are preferred to be found in dwarf galaxies hosting low-mass black holes (Wevers et al. 2022), this technique is particularly valuable as all previous methods are much less accurate in the low mass range (Greene et al. 2020). For example, the mass  $M_{\bullet}$  of the prototype and most well-studied intermediate-mass black hole (IMBH) in the nearby AGN NGC 4395 has a huge mass uncertainty between  $4 \times 10^5 M_{\odot}$  and  $1 \times 10^4 M_{\odot}$  reported by various works (Peterson et al. 2005; den Brok et al. 2015; Woo et al. 2019). In this regard, the QPE timing method we proposed will also aid in the detection of IMBHs with robust mass measurement, particularly in inactive galaxies throughout the universe.

Existing light curve data of QPEs have been obtained using XMM-Newton (Miniutti et al. 2019, 2023a,b; Arcodia et al. 2021; Arcodia et al. 2024a), Chandra (Miniutti et al. 2023b) and NICER (Arcodia et al. 2021; Chakraborty et al. 2024; Nicholl et al. 2024). Among these instruments, XMM-Newton provides the highest quality data but its observation epochs typically span only about one day. The precision of mass measurement is expected to improve substantially with extended-duration monitoring.

The Chasing All Transients Constellation Hunters (CATCH) (Li et al. 2023), proposed by the Institute of High Energy Physics at the Chinese Academy of Sciences, comprises a constellation of  $\mathcal{O}(10^2)$  satellites aiming to conduct simultaneous follow-up observations for diverse transients in the X-ray band. On June 22, 2024, the first CATCH pathfinder (Huang et al. 2024) was launched alongside the Space-based multiband astronomical Variable Objects Monitor (SVOM) mission (Götz et al. 2009). The complete constellation is projected to be deployed in the early 2030s. CATCH uses the WALKER constellation design with 3 orbital planes, each of which consists of a few tens of satellites. This configuration enables uninterrupted (long-term) monitoring mode (Li et al. 2023), effectively allowing continuous observation of a source. In this letter, we forecast the potential contribution of CATCH to the  $M_{\bullet}$  measurement and compare its capabilities with those of current instruments.

This Letter is organized as follows. In Section 2, we illustrate the underlying principles of the QPE timing method. In Section 3, we introduce the details of the Bayesian framework for QPE timing analysis. In Section 4, we simulate four strategies to demonstrate the capability of measuring  $M_{\bullet}$  of QPE timing method and two more strategies to demonstrate the unique potential of CATCH to measure  $a$ . Summary and discussions are given in Section 5. Throughout this paper, we will use geometric units with convention  $G = c = 1$ .

## 2. BASIC PRINCIPLES OF THE QPE TIMING METHOD

The physical picture of constraining the SMBH mass from QPE timing is rather simple. As the SMO orbiting around the SMBH, it crosses the accretion disk twice and produces two flares per orbit. Therefore, there is an alternating long-short pattern in the QPE recurrence times, arising from the orbital eccentricity and different light path length from the two collision locations to the observer. The orbital period can be identified as  $T_{\text{obt}} = T_{\text{long}} + T_{\text{short}}$  to a good precision, where  $T_{\text{long}}$  and  $T_{\text{short}}$  are the adjacent QPE recurrence times. Different from in Newtonian gravity, the EMRI orbit in the curved spacetime does not close itself due to the apsidal precession. As a result, both  $T_{\text{long}}$  and  $T_{\text{short}}$  are time dependent and vary on the timescale of the apsidal precession period  $T_{\text{aps}}$ . Both periods  $T_{\text{obt}}$  and  $T_{\text{aps}}$  can be constrained with a reasonable amount of QPE timing data, and are related to the SMBH mass  $M_{\bullet}$  and the semi-major axis  $A$  of the EMRI orbit via the Kepler's third law

$$T_{\text{obt}} = 2\pi \left( \frac{A}{M_{\bullet}} \right)^{3/2} M_{\bullet}, \quad (1)$$

and the ratio

$$\frac{T_{\text{aps}}}{T_{\text{obt}}} = \frac{p}{3M_{\bullet}} \approx \frac{A}{3M_{\bullet}}, \quad (2)$$

where  $p$  is the semi-latus rectum relating to the semi-major axis  $A$  and the orbital eccentricity  $e$  as  $A = p/(1 - e^2)$ , the approximation sign in the equation above is accurate for low-eccentricity orbits. With the two observables  $T_{\text{obt}}$  and  $T_{\text{aps}}$ , one can naturally constrain the SMBH mass with  $M_{\bullet} \propto T_{\text{obt}}^{5/2} T_{\text{aps}}^{-3/2}$ .

Note that the two periods measured in the observer frame are different from their intrinsic values by a factor of  $(1 + z)$  due to the cosmology redshift  $z$ , therefore the SMBH mass  $M_{\bullet}$  derived above is in fact a redshifted mass, which is different from the intrinsic mass by a factor of  $(1 + z)$ . The differences are small for currently detected QPE sources at low redshifts  $z \sim \mathcal{O}(0.01)$ , but could be important for sources at high redshifts.

In a similar way, one can constrain the Lense-Thirring precession period  $T_{\text{LT}}$  of the EMRI orbit from the QPE timing data if the QPE source has been monitored for a sufficiently long time  $\gtrsim T_{\text{LT}}$ . Consequently, one can infer the dimensionless spin  $a$  of the SMBH via the relation

$$\frac{T_{\text{LT}}}{T_{\text{obt}}} = \frac{1}{2a} \left( \frac{p}{M_{\bullet}} \right)^{3/2}. \quad (3)$$

In practice, we choose to conduct the QPE timing analysis in the Bayesian framework, the basic ingredients of which have been shown in previous works (papers I-III). In this work, we aim to generalize the previous analyses and construct a QPE

timing method which is capable of measuring orbital parameters and SMBH masses  $M_{\bullet}$  (and spins  $a$ ) in a comprehensive Bayesian framework.

## 3. BAYESIAN FRAMEWORK FOR QPE TIMING ANALYSIS

As discussed in previous studies, one can predict the SMO-disk collision times and the resulting QPE light curve with a model of SMO motion and an accretion disk model. But the full light prediction is subject to large uncertainties in the disk model, the nature of the SMO and the radiation mechanism. We therefore choose to constrain the EMRI kinematics and the QPE emission separately for mitigating the impact of these uncertainties. We first fit each QPE with a simple light curve model and obtain the starting time of each flare  $t_0 \pm \sigma(t_0)$  (see papers I-III for details), which is identified as the time of the SMO crossing the disk and is used for constraining the SMO orbital parameters. With data  $d = \{t_0^{(k)} \pm \sigma^{(k)}(t_0)\}$  ( $k$  is the flare index) and a QPE flare timing model, we can constrain model parameters  $\Theta$  in the Bayesian inference framework. According to the Bayes theorem, the posterior of model parameters is written as

$$\mathcal{P}(\Theta, \mathcal{H}|d) = \frac{\mathcal{L}(d|\Theta, \mathcal{H})\pi(\Theta, \mathcal{H})}{\mathcal{Z}(d)}, \quad (4)$$

where  $\mathcal{L}(d|\Theta, \mathcal{H})$  is the likelihood of detecting data  $d$  under hypothesis  $\mathcal{H}$  with model parameters  $\Theta$ ,  $\pi(\Theta, \mathcal{H})$  is the assumed prior for model parameters  $\Theta$  in  $\mathcal{H}$ , and the normalization factor  $\mathcal{Z}(d)$  is the evidence of hypothesis  $\mathcal{H}$  with data  $d$ .

To quantify the support for one hypothesis  $\mathcal{H}_1$  over another  $\mathcal{H}_0$  by data  $d$ , we can calculate the evidence ratio of two hypotheses, i.e., the Bayes factor,

$$\mathcal{B}_0^1 = \frac{\mathcal{Z}_1(d)}{\mathcal{Z}_0(d)}. \quad (5)$$

The larger  $\mathcal{B}_0^1$  represents stronger support for hypothesis  $\mathcal{H}_1$  over  $\mathcal{H}_0$ . In Jeffreys' scale,  $\log \mathcal{B}_0^1 \in (1.2, 2.3), (2.3, 3.5), (3.5, 4.6), (4.6, \infty)$  are the criteria of substantial, strong, very strong, and decisive strength of evidence, respectively.

In the following subsections, we will explain the two major components of the QPE timing model (EMRI trajectories and disk motion), define the likelihood for the Bayesian framework of the QPE timing method for measuring SMBH masses.

### 3.1. Forced EMRI trajectories

As shown in paper III, the SMO orbital energy dissipation as crossing the accretion disk is small but can be measured in some QPE sources via long term monitoring. In this subsection, we briefly review the steps of computing forced EMRI

trajectories in the Kerr spacetime. We start from time-like geodesics in the Kerr spacetime, analytic solutions to which have been derived by [Fujita & Hikida \(2009\)](#) and [van de Meent \(2020\)](#) as

$$\begin{aligned} r(\lambda) &= r(q_r(\lambda); E, L, C), & q_r(\lambda) &= \Upsilon_r \lambda + q_{r,\text{ini}}, \\ z(\lambda) &= z(q_z(\lambda); E, L, C), & q_z(\lambda) &= \Upsilon_z \lambda + q_{z,\text{ini}}, \\ t(\lambda) &= t(q_{t,r,z}(\lambda); E, L, C), & q_t(\lambda) &= \Upsilon_t \lambda + q_{t,\text{ini}}, \\ \phi(\lambda) &= \phi(q_{\phi,r,z}(\lambda); E, L, C), & q_\phi(\lambda) &= \Upsilon_\phi \lambda + q_{\phi,\text{ini}}, \end{aligned} \quad (6)$$

where  $\lambda$  is the Mino time;  $\{E, L, C\}$  are the energy, angular momentum and the Carter constant, respectively;  $\{\Upsilon_r, \Upsilon_z, \Upsilon_t, \Upsilon_\phi\}$  are the Mino time frequencies in the  $r, z (= \cos \theta), t, \phi$  direction, respectively;  $\{q_{r,\text{ini}}, q_{z,\text{ini}}, q_{t,\text{ini}}, q_{\phi,\text{ini}}\}$  are the initial phases. The conversion relation between the constants  $\{E, L, C\}$  and the orbital parameters  $\{p, e, \cos \theta_{\min}\}$  can be found in [Schmidt \(2002\)](#), where  $\theta_{\min}$  is the minimum polar angle that the geodesic can reach. A geodesic is uniquely determined by a set of orbital parameters  $\{p, e, \cos \theta_{\min}\}$  and initial phases  $\{q_{r,\text{ini}}, q_{z,\text{ini}}, q_{\phi,\text{ini}}\}$  at initial time  $t_{\text{ini}}$ , where the initial phase  $q_{t,\text{ini}}$  is fixed by  $t(q_{t,\text{ini}}, q_{r,\text{ini}}, q_{z,\text{ini}}) = t_{\text{ini}}$ .

Assuming the orbital energy dissipation as the SMO crosses the accretion disk is a small perturbation, then the SMO trajectories can be formulated as perturbed geodesics with varying constants  $\{E(t), L(t), C(t)\}$ . In the language of perturbation techniques, the forced EMRI trajectories can be computed using the method of osculating orbits, i.e., in the adiabatic approximation, the equations of motion can be written as

$$\begin{aligned} r(\lambda) &= r(q_r(\lambda); E, L, C), & \frac{dq_r}{d\lambda} &= \Upsilon_r(E, L, C), \\ z(\lambda) &= z(q_z(\lambda); E, L, C), & \frac{dq_z}{d\lambda} &= \Upsilon_z(E, L, C), \\ t(\lambda) &= t(q_{t,r,z}(\lambda); E, L, C), & \frac{dq_t}{d\lambda} &= \Upsilon_t(E, L, C), \\ \phi(\lambda) &= \phi(q_{\phi,r,z}(\lambda); E, L, C), & \frac{dq_\phi}{d\lambda} &= \Upsilon_\phi(E, L, C), \end{aligned} \quad (7)$$

with time-dependent  $\{E, L, C\}$  and thereby time-dependent frequencies  $\Upsilon_{r,z,t,\phi}$ .

The time dependence of  $\{E, L, C\}$  can be derived from the change of orbital parameters of  $\{T_{\text{obt}}(p, e), e, \cos \theta_{\min}\}$  as the SMO crosses the disk. As shown in several recent studies of star-disk collisions (e.g., [Linial & Metzger 2023a](#); [Wang et al. 2023b](#)), the relative changes in orbital parameters are similar in magnitudes with  $\delta e/e \sim \delta T_{\text{obt}}/T_{\text{obt}} \sim \delta \theta_{\min}/\theta_{\min}$ . As we have shown in previous studies,  $T_{\text{obt}}$  is the best constrained orbital parameter while  $e$  and  $\cos \theta_{\min}$  are less constrained with  $O(1)$  fractional uncertainties. As a result, the small fractional change in the orbital period  $\delta T_{\text{obt}}$  is detectable, while

$\delta e$  and  $\delta \theta_{\min}$  are undetectable for the QPE sources currently available. We therefore can safely take  $\dot{e} = \dot{\theta}_{\min} = 0$  in calculating the EMRI trajectories. As for the orbital period decay rate  $\dot{T}_{\text{obt}}(t)$ , we model it as

$$\dot{T}_{\text{obt}}(t) = \dot{T}_{\text{obt,max}} \sin \iota_{\text{sd}}(t), \quad (8)$$

where  $\iota_{\text{sd}}$  the angle between the SMO orbital plane and the disk plane. This function form is motivated by the energy loss for a star crossing an accretion disk ([Linial & Quataert 2023](#); [Linial & Metzger 2023a](#)). For a precessing misaligned disk,  $\iota_{\text{sd}}$  is modulated by the disk precession and the SMO orbital precession, therefore the decay rate  $\dot{T}_{\text{obt}}$  is non-uniform. In the case of an equatorial accretion disk, the orbital period decay rate simplifies as a constant.

### 3.2. Disk motion: precession and alignment

In general, a TDE star that is scattered into the tidal radius of a SMBH is from a random direction. As a result, the initial orientation of the accretion disk formed in a TDE is also random. The possible signature of the disk precession on the QPE timing has been discussed in several previous studies (e.g., [Franchini et al. 2023](#); [Chakraborty et al. 2024](#); [Arcodia et al. 2024a](#); [Miniutti et al. 2024](#)). As a minimal assumption of the disk precession, we model it as a rigid body like precession with a constant precession rate. The normal vector of the disk plane is written as

$$\vec{n}_{\text{disk}} = (\sin \beta \cos \alpha, \sin \beta \sin \alpha, \cos \beta), \quad (9)$$

where  $\alpha \in (0, 2\pi)$  is the azimuth angle and  $\beta \in (0, \pi/2)$  is the angle between the disk plane and the equatorial plane. With the constant precession rate assumption, the azimuth angle then evolves as

$$\alpha(t) = \alpha_{\text{ini}} + \frac{2\pi}{\tau_p}(t - t_{\text{ini}}), \quad (10)$$

where  $\tau_p$  is the disk precession period, and  $\alpha_{\text{ini}}$  is the initial value of the azimuth angle at  $t_{\text{ini}}$ .

In the long run, the initially misaligned disk is expected to approach the equator plane gradually. One can in principle constrain the evolution history of the inclination angle  $\beta(t)$  in a non-parametric approach if sufficiently dense observations of QPEs are available. However, QPE sources are usually sparsely monitored due to limited X-ray observation resources. In practice, we choose to bridge the sparse observations with a simple function

$$\sin \beta(t) = \sin \beta_{\text{ini}} \exp \left\{ -\frac{t - t_{\text{ini}}}{\tau_a} \right\}, \quad (11)$$

parameterizing the alignment process with the alignment timescale parameter  $\tau_a$ , where  $\beta_{\text{ini}}$  is the initial value of the disk inclination angle. This function form is motivated by the eigen-mode analysis of disk alignment process (e.g., [Scheuer & Feiler 1996](#); [Zanazzi & Lai 2019](#)).



### 3.3. QPE timing model

In the previous two subsections, we have summarized the key points in modeling the EMRI motion and the disk motion, based on which one can construct a full QPE timing model. But not all the ingredients are necessary for modeling each QPE source, e.g., no evidence for disk precession in GSN 069 QPEs is found (Zhou et al. 2024a). Therefore we consider the following two hypotheses with slightly different assumptions about the EMRI motion and the disk motion, and the data favored hypothesis will be selected by Bayesian analyses:

- Vanilla hypothesis ( $\mathcal{H}_0$ ): The SMO moves around the SMBH losing orbital energy as crossing the equatorial accretion disk. The EMRI+disk system can be specified by 9 parameters: the intrinsic orbital parameters ( $p, e, \theta_{\min}$ ), the initial phases ( $q_{r,\text{ini}}, q_{z,\text{ini}}, q_{\phi,\text{ini}}$ ), the mass of the SMBH  $M_\bullet$  or equivalently the orbital period  $T_{\text{obt}}$  [Eq. (1)], the dimensionless spin of the SMBH  $a$  and the orbital period decay rate  $\dot{T}_{\text{obt}}$ .
- Disk precession and alignment hypothesis ( $\mathcal{H}_1$ ): Different from the vanilla hypothesis, we consider a misaligned disk with initial orientation angles ( $\alpha_{\text{ini}}, \beta_{\text{ini}}$ ) and precessing around the polar direction with a constant period  $\tau_p$ . In this hypothesis, the angle between the SMO orbital plane and the accretion disk  $\iota_{\text{sd}}$  is time dependent, so does the orbital period decay rate [Eq. (8)]. In addition to disk precession, we also consider a possible disk alignment process which is parameterized with an alignment timescale  $\tau_a$  [Eq. (11)]. Therefore, 4 additional parameters  $\{\alpha_{\text{ini}}, \beta_{\text{ini}}, \tau_p, \tau_a\}$  are introduced for describing the disk motion in this hypothesis (and the orbital period decay rate parameter  $\dot{T}_{\text{obt}}$  in  $\mathcal{H}_0$  is replaced with  $\dot{T}_{\text{obt,max}}$ ).

From a SMO trajectory and disk motion, one can calculate the disk crossing times  $t_{\text{crs}}$ , which we identify as the flare starting times. Specifically, we choose the disk crossing time as when the SMO crosses the upper disk surface or the lower disk surface depending on the observer direction, i.e.  $r_{\text{crs}}(\vec{n}_{\text{crs}} \cdot \vec{n}_{\text{disk}}) = H \text{sign}(\vec{n}_{\text{obs}} \cdot \vec{n}_{\text{disk}})$ . Without loss of generality, we fix the observer in the  $x-z$  plane, i.e., the unit direction vector pointing to the observer is  $\vec{n}_{\text{obs}} = (\sin \theta_{\text{obs}}, 0, \cos \theta_{\text{obs}})$ . The propagation times of different flares at different collision locations  $r_{\text{crs}} \vec{n}_{\text{crs}}$  to the observer will also be different. Taking the light propagation delays into account, we find the flare starting time in the observer frame as

$$t_{\text{obs}} = t_{\text{crs}} + \delta t_{\text{geom}} + \delta t_{\text{shap}}, \quad (12)$$

where

$$\begin{aligned} \delta t_{\text{geom}} &= -r_{\text{crs}} \vec{n}_{\text{obs}} \cdot \vec{n}_{\text{crs}}, \\ \delta t_{\text{shap}} &= -2M_\bullet \log[r_{\text{crs}}(1 + \vec{n}_{\text{obs}} \cdot \vec{n}_{\text{crs}})], \end{aligned} \quad (13)$$

are corrections caused by different light path lengths and different Shapiro delays (Shapiro 1964), respectively. To summarize, our QPE timing model is written as  $t_{\text{obs}}^{(k)}(\Theta, \mathcal{H})$  in a short notation, where  $k$  is the index of observed flares,  $\mathcal{H}$  is the hypothesis adopted and  $\Theta$  is the associated model parameters.

### 3.4. Bayesian framework

As discussed in previous analyses, it is possible that there are some physical processes that affect the QPE timing but are not included in our QPE timing model. Assuming the unmodeled advances or delays in the QPE timing follows a Gaussian distribution with variance  $\sigma_{\text{sys}}^2$ , the likelihood of seeing data  $d = \{t_0^{(k)}\}$  under hypothesis  $\mathcal{H}$  with model parameters  $\Theta$  is written as (see paper II for a short derivation)

$$\mathcal{L}_{\text{timing}}(d|\Theta, \mathcal{H}) = \prod_k \frac{1}{\sqrt{2\pi(\tilde{\sigma}(t_0^{(k)}))^2}} \exp\left\{-\frac{(t_{\text{obs}}^{(k)} - t_0^{(k)})^2}{2(\tilde{\sigma}(t_0^{(k)}))^2}\right\}, \quad (14)$$

where  $(\tilde{\sigma}(t_0^{(k)}))^2 = (\sigma(t_0^{(k)}))^2 + \sigma_{\text{sys}}^2$  is the uncertainty contributed by both measurement errorbars and unmodeled uncertainties. Note that  $\Theta$  includes both the physical parameters introduced in the previous subsection and the systematic uncertainty parameter  $\sigma_{\text{sys}}$ . Similar inference method has been widely used in the context of hierarchical test of General Relativity with gravitational waves (Isi et al. 2019).

For each QPE source, we apply both hypotheses  $\mathcal{H}_{0,1}$  to the timing data of observed flares  $t_0^{(k)}$ , and perform model parameter inferences using the *nessai* (Williams 2021) algorithm within *Bilby* (Ashton et al. 2019). As we will see later, the data favored hypothesis will be featured with higher evidence obtained from the Bayesian inference, and the hypothesis preference is quantified by the Bayes factor.

As a clean measurement of the SMBH mass from QPE timing data alone, we do not include any prior information about the SMBH mass informed by external measurements, e.g., commonly used  $M_\bullet - \sigma_\star$  relations (Tremaine et al. 2002; Gültekin et al. 2009).

## 4. APPLICATIONS OF THE QPE TIMING METHOD

### 4.1. GSN 069

We first apply the comprehensive Bayesian framework to the well-studied QPE source, GSN 069, which has been extensively analyzed in paper I-III. In Table 1, we present the priors of model parameters used for orbital analyses in  $\mathcal{H}_0$ ,  $\mathcal{H}_1$ . The orbital parameters are constrained as

$$\begin{aligned} p &= 305_{-59}^{+50} M_\bullet, \\ e &= 0.04_{-0.02}^{+0.02}, \quad (\mathcal{H}_0) \\ T_{\text{obt}} &= 64.73_{-0.03}^{+0.02} \text{ ks}, \\ \dot{T}_{\text{obt}} &= -6.5_{-0.2}^{+0.2} \times 10^{-5}, \end{aligned} \quad (15)$$

$\Theta$	$\pi(\Theta, \mathcal{H}_1)$	$\pi(\Theta, \mathcal{H}_0)$
$p [M_\bullet]$	$\mathcal{U}[50, 500]$	
$e$	$\mathcal{U}[0, 0.9]$	
$\cos(\theta_{\min})$	$\mathcal{U}[0, 1]$	
$q_{r,\text{ini}}$	$\mathcal{U}[0, 2\pi]$	
$q_{z,\text{ini}}$	$\mathcal{U}[0, 2\pi]$	
$q_{\phi,\text{ini}}$	$\mathcal{U}[0, 2\pi]$	
$T_{\text{obt}} [\text{ks}]$	$\mathcal{U}[60, 70]$	
$a$	$\mathcal{U}[0, 1]$	
$\theta_{\text{obs}}$	$\mathcal{U}[0, \pi]$	$\mathcal{U}[0, \pi/2]$
$\alpha_{\text{ini}}$	$\mathcal{U}[0, 2\pi]$	None
$\tau_p [\text{days}]$	$\mathcal{U}[1, 2000]$	None
$\beta_{\text{ini}}$	$\mathcal{U}[0, \pi/2]$	None
$\tau_a [\text{days}]$	$\mathcal{U}[1, 2000]$	None
$\dot{T}_{\text{obt}} [\times 10^{-5}]$	None	$\mathcal{U}[-10, 0]$
$\dot{T}_{\text{obt,max}} [\times 10^{-5}]$	$\mathcal{U}[-10, 0]$	None
$\sigma_{\text{sys}} [\text{ks}]$	$\mathcal{U}[0, 2]$	

**Table 1.** Priors used for the orbital parameter inference of GSN 069 EMRI. Entries left blank in the  $\pi(\Theta, \mathcal{H}_0)$  column indicate that the same prior values from the  $\pi(\Theta, \mathcal{H}_1)$  column are imposed.

and

$$\begin{aligned}
 p &= 355_{-83}^{+79} M_\bullet, \\
 e &= 0.04_{-0.02}^{+0.01}, \\
 T_{\text{obt}} &= 64.56_{-0.13}^{+0.14} \text{ ks}, \quad (\mathcal{H}_1) \\
 \dot{T}_{\text{obt,max}} &= -7.6_{-1.5}^{+3.5} \times 10^{-5}, \\
 \tau_p &= 274_{-108}^{+955} \text{ days}, \\
 \tau_a &= 709_{-524}^{+659} \text{ days},
 \end{aligned} \tag{16}$$

at 2- $\sigma$  confidence level. The log Bayes factor between the two hypotheses is found to be

$$\log \mathcal{B}_0^1 = -2.6 \pm 0.2. \tag{17}$$

This shows that an equatorial disk in GSN 069 is strongly favored and there is no evidence for disk precession.

The SMBH mass constraint in the data favored hypothesis is found to be

$$\log_{10}(M_\bullet/M_\odot) = 5.6_{-0.1}^{+0.1}, \quad (\mathcal{H}_0) \tag{18}$$

at 2- $\sigma$  confidence level. This constraint is independent of and of significantly lower uncertainty than the constraint inferred from the  $M_\bullet - \sigma_\star$  relation,  $\log_{10}(M_\bullet/M_\odot) = 6.0 \pm 1.0$  (at 2- $\sigma$  confidence level) (Wevers et al. 2022). GSN 069 represents a good example of dynamical measurement of SMBH masses with the QPE timing method.

#### 4.2. Optimal observation strategy: SMBH mass measurement

In this subsection, we simulate different strategies of observing QPEs and evaluate their performances in measuring SMBH masses. As an example, we consider a mock

$\Theta$	$\pi(\Theta, \mathcal{H}_0)$	injection values
$p [M_\bullet]$	$\mathcal{U}[50, 1000]$	100
$e$	$\mathcal{U}[0, 0.9]$	0.04
$\cos(\theta_{\min})$	$\mathcal{U}[0, 1]$	0.5
$q_{r,\text{ini}}$	$\mathcal{U}[0, 2\pi]$	1.4 $\pi$
$q_{z,\text{ini}}$	$\mathcal{U}[0, 2\pi]$	1.6 $\pi$
$q_{\phi,\text{ini}}$	$\mathcal{U}[0, 2\pi]$	0.3 $\pi$
$T_{\text{obt}} [\text{ks}]$	$\mathcal{U}[20, 40]$	31.5
$a$	$\mathcal{U}[0, 1]$	0.9
$\theta_{\text{obs}}$	$\mathcal{U}[0, \pi/2]$	$\pi/3$
$\dot{T}_{\text{obt}} [\times 10^{-5}]$	$\mathcal{U}[-10, 0]$	-1
$\sigma_{\text{sys}} [\text{ks}]$	$\mathcal{U}[0, 2]$	0

**Table 2.** Priors and the injection values of the QPE timing model parameters used for the simulations.

QPE source that is similar to GSN 069 and eRO-QPE2, with source parameters  $M_\bullet = 10^6 M_\odot$ ,  $a = 0.9$ ,  $p = 100 M_\bullet$ ,  $e = 0.04$ . The three dynamical timescales are therefore  $T_{\text{obt}} = 31.5 \text{ ks}$ ,  $T_{\text{aps}} = 12.1 \text{ days}$  and  $T_{\text{LT}} = 202.5 \text{ days}$ . For convenience, we assume an equatorial disk and the injection values of full QPE timing model parameters are listed in Table 2.

Using the osculating trajectory method described above, true flare starting times in the observer frame  $t_{\text{obs,true}}^{(k)}$  are calculated directly following Eq. (12). The observed flare starting times  $t_0^{(k)}$  will be slightly different due to measurement noises,

$$t_0^{(k)} = t_{\text{obs,true}}^{(k)} + \delta t_0^{(k)}, \tag{19}$$

where  $\delta t_0^{(k)}$  is randomly drawn from a Gaussian distribution with a mean value 0 and a standard deviation  $\sigma(t_0^{(k)})$ . In this work, we fix the measurement uncertainty as  $\sigma(t_0^{(k)}) = 100 \text{ s}$ , a typical value found in previous QPE data analyses.

Different from traditional X-ray telescopes, CATCH consists of  $\mathcal{O}(10^2)$  small satellites which enable uninterrupted long timescale monitoring of multiple targets. As a reference, we first consider an uninterrupted observation epoch lasting for one apsidal precession period  $T_{\text{aps}} \approx 12 \text{ days}$ , then two different strategies of observation cadence and duration of each observation epoch if the total amount of observation time is fixed as  $T_{\text{obs}} = 4 \text{ days}$ .

- Strategy A: A single uninterrupted observation epoch lasting for one apsidal precession period  $T_{\text{aps}} \approx 12 \text{ days}$ .
- Strategy B: Four observation epochs distributed randomly in 12 days, with each epoch lasting for 1 day.
- Strategy C: Same to B, except for the epochs distributed randomly in  $\sim 50 \text{ days}$ , mimicking existing QPE observations, e.g., observations of GSN 069 during Dec. 2018-May 2019 (Fig. 1).

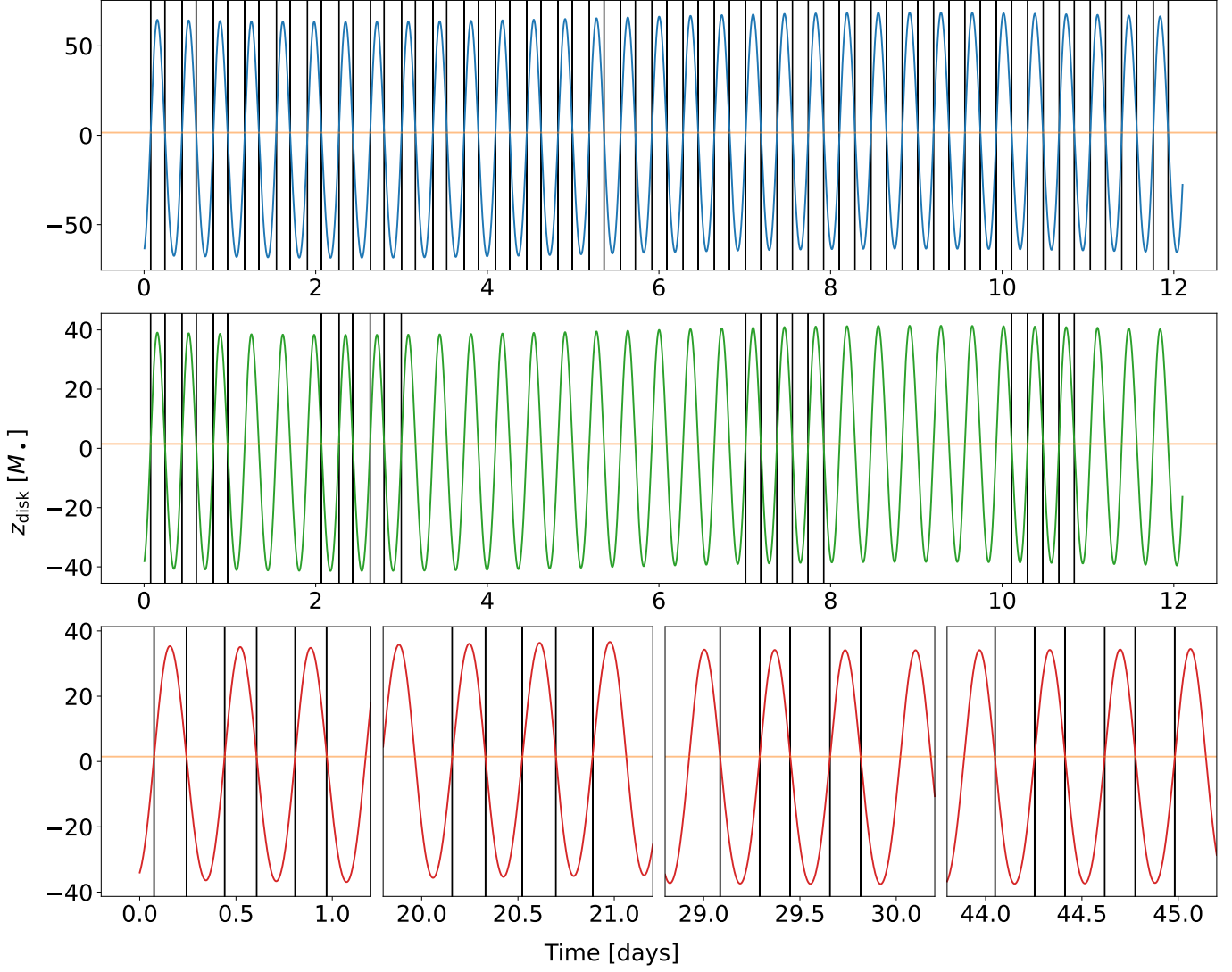


**Figure 3.** Best-fit EMRI trajectories obtained with three different strategies, where  $z_{\text{disk}}(t)$  is the  $z$ -component. The vertical bands indicate the simulated data  $t_0^{(k)} \pm \sigma(t_0^{(k)})$ . The orange horizontal line marks the disk surface. Blue: strategy A. Green: strategy B. Red: strategy C.

From mock observations of Strategies A, B and C, we infer model parameters as in the case of GSN 069. The model parameter priors used are listed in Table 2. The inferred values of the semi-latus rectum  $p$ , eccentricity  $e$ , orbital period  $T_{\text{orb}}$ , apsidal precession period  $T_{\text{aps}}$  and SMBH mass  $M_{\bullet}$  from the three strategies are summarized in Table 3. The best-fit EMRI trajectories under the three strategies are shown in Fig. 3.

Specifically, we show the posteriors of the apsidal precession period  $T_{\text{aps}}$  in Fig. 4. It is of no surprise to find uninterrupted monitoring for a long timescale ( $\sim 12$  days) in Strategy A yields the tightest constraints on  $T_{\text{aps}}$  and consequently on the SMBH mass  $M_{\bullet}$ . If the total observation time is limited, observation cadence and duration of each observation epoch make a difference. Strategy B and C are similar except different observation cadence, which yield quite differ-

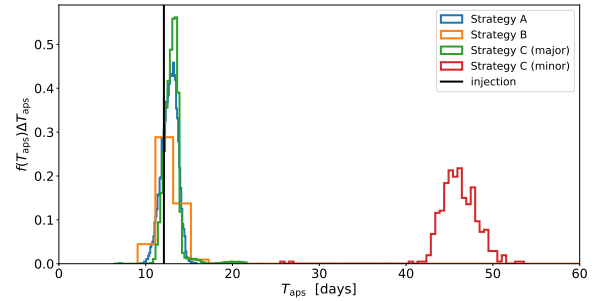


**Figure 4.** Probability distributions  $f(T_{\text{aps}})\Delta T_{\text{aps}}$  of the apsidal precession period  $T_{\text{aps}}$  obtained from three different observation strategies, where  $\Delta T_{\text{aps}}$  is the bin size.

ent  $T_{\text{aps}}$  constraints. Strategy B of high observation cadence also yields a reasonable constraint, wider than in Strategy A



Strategy for mass measurement	$p [M_\bullet]$	$e$	$T_{\text{obt}} [\text{ks}]$	$T_{\text{aps}} [\text{day}]$	$\log_{10}(M_\bullet/M_\odot)$
A	$106^{+12}_{-16}$	$0.04^{+0.00}_{-0.01}$	$31.5^{+0.03}_{-0.06}$	$12.8^{+1.5}_{-2.0}$	$5.97^{+0.11}_{-0.07}$
B	$104^{+29}_{-18}$	$0.04^{+0.01}_{-0.01}$	$31.5^{+0.04}_{-0.07}$	$12.6^{+3.5}_{-2.2}$	$5.98^{+0.12}_{-0.16}$
C (major/minor)	$107^{+19}_{-13}/378^{+34}_{-26}$	$0.05^{+0.02}_{-0.02}$	$31.5^{+0.03}_{-0.06}$	$13.1^{+2.4}_{-1.6}/46.0^{+4.1}_{-3.1}$	$5.95^{+0.08}_{-0.11}/5.13^{+0.05}_{-0.06}$

**Table 3.** Median values and  $2\text{-}\sigma$  uncertainties of semi-latus rectum  $p$ , eccentricity  $e$ , orbital period  $T_{\text{obt}}$ , apsidal precession period  $T_{\text{aps}}$  and SMBH mass  $M_\bullet$  for the three strategies considered.

by a factor of  $\sim \sqrt{3}$ . In contrast, Strategy C of low observation cadence yields double-peak structure in the posterior of  $T_{\text{aps}}$ , a major peak located at the injection value and a minor one at roughly four times the injection value. This result is also consistent with the intuition that the phase information encoded in each observation epoch adds up “coherently” if intervals between consecutive observations is short ( $\ll T_{\text{aps}}$ ).

For the purpose of precise measurement of SMBH masses from QPE timing, the optimal strategy is clearly strategy A, which consists of a single observation epoch that spans an entire apsidal precession period  $T_{\text{aps}}$ . However, QPE sources exhibit a wide range of  $T_{\text{aps}}$  from tens to hundreds of days. For sources of particular interest, such as eRO-QPE2 with  $T_{\text{aps}} \sim 1$  month, uninterrupted long-term monitoring over one full  $T_{\text{aps}}$  is feasible for CATCH. Nevertheless, this approach becomes impractical for sources with longer  $T_{\text{aps}}$ . A more practical alternative exemplified by strategy B is to divide the limited total observation time into  $N \approx T_{\text{obs}}/(2T_{\text{obt}})$  separate epochs, ensuring that each epoch captures at least  $\gtrsim 3$  QPE flares. To properly sample the phase information of apsidal precession, these epochs should be quasi-uniformly distributed within one  $T_{\text{aps}}$ , as exemplified in Strategy B.

#### 4.3. Optimal observation strategy: SMBH spin measurement

Similar to the apsidal precession, Lense-Thirring precession of the EMRI orbital plane in the Kerr spacetime also introduces a super-orbital modulation to the QPE recurrence times. In general, the Lense-Thirring precession period  $T_{\text{LT}}$  is much longer than both the orbital period  $T_{\text{obt}}$  and the apsidal precession period  $T_{\text{aps}}$ . Uninterrupted monitoring of QPE sources for a long period of time  $\sim T_{\text{LT}}$  seems impractical even for CATCH. To demonstrate the feasibility of the QPE timing method in measuring the SMBH spin with a limited amount of observation time  $T_{\text{obs}} \ll T_{\text{LT}}$ , we fix  $T_{\text{obs}} = 15$  days and simulate the following two observation strategies.

- Strategy I: 15 observation epochs with each epoch lasting for 1 day and distributed within  $T_{\text{LT}}$  in a quasi-uniform way.
- Standard II: 5 observation epochs with each epoch lasting for 3 days and distributed within  $T_{\text{LT}}$  in a quasi-uniform way.

We perform the Bayesian analysis as in the case of SMBH mass measurement simulations. The inferred values of the

semi-latus rectum  $p$ , eccentricity  $e$ , orbital period  $T_{\text{obt}}$ , apsidal precession period  $T_{\text{aps}}$ , Lense-Thirring precession period  $T_{\text{LT}}$ , SMBH mass  $M_\bullet$  and SMBH spin  $a$  from the two strategies are summarized in Table 4. The best-fit EMRI trajectories under the three strategies are shown in Fig. 5.

Although observations of low cadence are not able to resolve apsidal precession in strategy C, more observations as in strategy I, make a difference. If enough amount of separated observation epochs are distributed within one  $T_{\text{LT}}$ , strategy I demonstrates that  $T_{\text{LT}}$  can be resolved, which in turn improves the resolution of  $T_{\text{aps}}$ . Meanwhile, the strategy II with an even lower observation cadence yet longer single epoch duration within one  $T_{\text{LT}}$  achieves the same precision of  $M_\bullet$  and  $a$  measurement as in strategy I. Both strategy I and II reduce the  $2\text{-}\sigma$  uncertainty of  $\log_{10}(M_\bullet)$  by an order of magnitude compared to strategies A-C. The SMBH spin  $a$  is also well constrained with comparable  $2\text{-}\sigma$  uncertainties  $< 0.1$  in both strategies I and II. Strategy I with higher cadence yields tighter constraints on a fraction of model parameters ( $e, T_{\text{obt}}, T_{\text{aps}}$ ) than in strategy II.

A similar idea has also been proposed for measuring the Sgr A\* SMBH spin by tracing S stars (Zhang et al. 2015). For the star S2, the Lense-Thirring precession is out of reach of the current astrometry (Genzel et al. 2024). A star moving around the Sgr A\* on a tighter orbit is desired for detecting the SMBH spin from Lense-Thirring precession (Waisberg et al. 2018).

## 5. SUMMARY AND DISCUSSIONS

More and more analyses show that (at least a fraction of) QPEs are sourced by quasi-periodic collisions between SMOs and accretion disks of SMBHs. As a result, the QPE timing data encode rich information of the EMRI trajectory, including the orbital period  $T_{\text{obt}}$ , the apsidal precession period  $T_{\text{aps}}$  and the Lense-Thirring precession period  $T_{\text{LT}}$ , from which one can robustly measure the SMBH mass and spin. We name this dynamical measurement method as the QPE timing method, which is in the same spirit of measuring the Sagittarius A\* SMBH mass by tracing individual stars around the SMBH (Schödel et al. 2002; Ghez et al. 2005; Gillessen et al. 2009; GRAVITY Collaboration et al. 2018). The QPE timing method can be applied to a much broader range of SMBHs since there is no need to spatially resolve the orbits of individual stars.

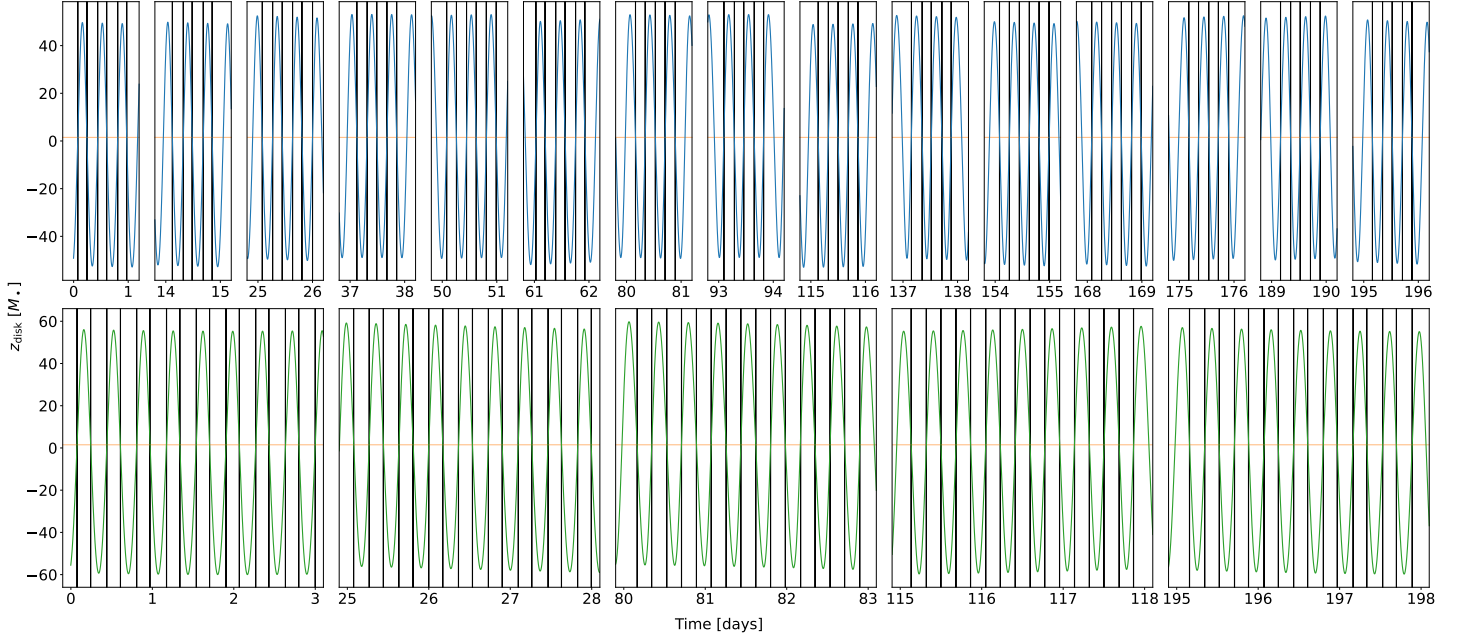


**Figure 5.** Same to Fig. 3 except for strategies to SMBH spin measurement. Blue: strategy I. Green: strategy II.

Strategy for spin measurement	$p [M_{\bullet}]$	$e$	$T_{\text{obt}} [\text{ks}]$	$T_{\text{aps}} [\text{day}]$	$T_{\text{LT}} [\text{day}]$	$\log_{10}(M_{\bullet}/M_{\odot})$	$a$
I	$100^{+1}_{-1}$	$0.04^{+0.005}_{-0.005}$	$31.5^{+0.005}_{-0.004}$	$12.1^{+0.1}_{-0.1}$	$203^{+22}_{-14}$	$6.00^{+0.01}_{-0.01}$	$0.89^{+0.07}_{-0.08}$
II	$101^{+3}_{-1}$	$0.04^{+0.01}_{-0.01}$	$31.5^{+0.01}_{-0.01}$	$12.2^{+0.3}_{-0.2}$	$213^{+24}_{-13}$	$6.00^{+0.01}_{-0.02}$	$0.86^{+0.06}_{-0.08}$

**Table 4.** Median values and  $2\text{-}\sigma$  uncertainties of semi-latus rectum  $p$ , eccentricity  $e$ , orbital period  $T_{\text{obt}}$ , apsidal precession period  $T_{\text{aps}}$ , Lense-Thirring precession period  $T_{\text{LT}}$ , SMBH mass  $M_{\bullet}$  and SMBH spin  $a$  for the two strategies considered.

To implement the QPE timing method, we constructed a comprehensive Bayesian inference framework in which one can reconstruct the EMRI trajectory (and the disk motion), consequently measure the SMBH parameters from QPE timing data.

As an example, we first applied the QPE timing method to the well-studied QPE source GSN 069, analyzing its orbital parameters under different hypotheses in the Bayesian inference framework. According to the log Bayes factor [Eq. (17)] between two different hypotheses, we found the disk precession hypothesis ( $\mathcal{H}_1$ ) is disfavored compared to the vanilla equatorial disk hypothesis ( $\mathcal{H}_0$ ). In the data favored  $\mathcal{H}_0$ , the SMBH mass is tightly constrained [Eq. (18)], with an uncertainty much lower than intrinsic uncertainties of  $M_{\bullet} - \sigma_{\star}$  relations. This example demonstrated the feasibility of the QPE timing method in reconstructing the EMRI trajectory and measuring the SMBH mass.

The QPE timing method opens up the possibility for precision measurement of SMBHs, though the current bottleneck is the limited X-ray observation resources available. The multi-target X-ray telescope under construction, CATCH (Li et al. 2023), will hopefully be the solution to the bottleneck of X-ray followup observation. First, CATCH will allow comprehensive X-ray monitoring of a large sample of opti-

cal TDEs in the era of the Rubin Observatory Legacy Survey of Space and Time (LSST, Ivezić et al. 2019) and the Wide Field Survey Telescope (WFST, Wang et al. 2023a), and thus the discovery of a large number of QPEs following TDEs. Refined observations can then be made for the QPE targets. In this work, we explored different observation strategies for accurately measuring SMBH masses from QPE timing in the CATCH era. In general, the apsidal precession period  $T_{\text{aps}}$  is much longer than the orbital period  $T_{\text{obt}}$ , therefore is harder to be accurately measured. As a result, the mass  $M_{\bullet}$  measurement precision is mainly determined by the measurement precision of the apsidal precession period, with

$$\frac{\delta M_{\bullet}}{M_{\bullet}} \approx \frac{3}{2} \frac{\delta T_{\text{aps}}}{T_{\text{aps}}}. \quad (20)$$

For particularly interesting QPE sources, the design of CATCH enables uninterrupted long-term (say  $\sim 1$  month) monitoring. This will of course be the optimal strategy for precision measurement of SMBH masses. For general QPE sources, we may allocate less total amount of observation time  $T_{\text{obs}}$ , and divide the total observation time into  $N \approx T_{\text{obs}}/(2T_{\text{obt}})$  epochs that are distributed in a quasi-uniform way within one apsidal precession period  $T_{\text{aps}}$ . In this way, each observation epoch guarantees to detect  $\gtrsim 3$

eruptions, and the apsidal precession information encoded in different epochs adds up “coherently”, therefore enables an optimal measurement of  $T_{\text{aps}}$  given a limited amount of total observation time.

The same strategy works for measuring the SMBH spin using the QPE timing method. The only difference is that a even longer timescale  $T_{\text{LT}}$  matters, which takes more observation time to be measured. The spin measurement precession is up to the measurement precision of the Lense-Thirring precession period  $T_{\text{LT}}$  with

$$\frac{\delta a}{a} \approx \frac{\delta T_{\text{LT}}}{T_{\text{LT}}} . \quad (21)$$

In practice, the apsidal precession period  $T_{\text{aps}}$  and the Lense-Thirring precession period  $T_{\text{LT}}$  are unknown *a priori*. Therefore, the observation strategy and the model parameter inference can only be updated iteratively.

1 We thank Yue Liao for helping making the schematic pic-  
2 ture in Fig. 2. This work is supported by the Strategic Prior-  
3 ity Research Program of the Chinese Academy of Sciences  
4 (XDB0550200), the National Natural Science Foundation of  
5 China (grants 12192221,12393814) and the China Manned  
6 Space Project.

## REFERENCES

- Abuter, R., Allouche, F., Amorim, A., et al. 2024, *Nature*, 627, 281, doi: [10.1038/s41586-024-07053-4](https://doi.org/10.1038/s41586-024-07053-4)
- Arcodia, R., Merloni, A., Nandra, K., et al. 2021, *Nature*, 592, 704, doi: [10.1038/s41586-021-03394-6](https://doi.org/10.1038/s41586-021-03394-6)
- Arcodia, R., Miniutti, G., Ponti, G., et al. 2022, *Astronomy&Astrophysics*, 662, A49, doi: [10.1051/0004-6361/202243259](https://doi.org/10.1051/0004-6361/202243259)
- Arcodia, R., Liu, Z., Merloni, A., et al. 2024, arXiv e-prints, arXiv:2401.17275, doi: [10.48550/arXiv.2401.17275](https://doi.org/10.48550/arXiv.2401.17275)
- Arcodia, R., et al. 2024a. <https://arxiv.org/abs/2406.17020>
- Arcodia, R., Merloni, A., Buchner, J., et al. 2024b. <https://arxiv.org/abs/2403.17059>
- Ashton, G., Hübner, M., Lasky, P. D., et al. 2019, *Astroph.J.S.*, 241, 27, doi: [10.3847/1538-4365/ab06fc](https://doi.org/10.3847/1538-4365/ab06fc)
- Bykov, S., Gilfanov, M., Sunyaev, R., & Medvedev, P. 2024. <https://arxiv.org/abs/2409.16908>
- Chakraborty, J., Kara, E., Masterson, M., et al. 2021, *Astroph.J.Lett.*, 921, L40, doi: [10.3847/2041-8213/ac313b](https://doi.org/10.3847/2041-8213/ac313b)
- Chakraborty, J., Arcodia, R., Kara, E., et al. 2024, arXiv e-prints, arXiv:2402.08722, doi: [10.48550/arXiv.2402.08722](https://doi.org/10.48550/arXiv.2402.08722)
- Chakraborty, J., et al. 2025. <https://arxiv.org/abs/2503.19013>
- den Brok, M., Seth, A. C., Barth, A. J., et al. 2015, *ApJ*, 809, 101, doi: [10.1088/0004-637X/809/1/101](https://doi.org/10.1088/0004-637X/809/1/101)
- Evans, P. A., Nixon, C. J., Campana, S., et al. 2023, *Nature Astronomy*, 7, 1368, doi: [10.1038/s41550-023-02073-y](https://doi.org/10.1038/s41550-023-02073-y)
- Ferrarese, L., & Merritt, D. 2000, *Astroph.J.Lett.*, 539, L9, doi: [10.1086/312838](https://doi.org/10.1086/312838)
- Franchini, A., Bonetti, M., Lupi, A., et al. 2023, *Astronomy&Astrophysics*, 675, A100, doi: [10.1051/0004-6361/202346565](https://doi.org/10.1051/0004-6361/202346565)
- Fujita, R., & Hikida, W. 2009, *Class. Quant. Grav.*, 26, 135002, doi: [10.1088/0264-9381/26/13/135002](https://doi.org/10.1088/0264-9381/26/13/135002)
- Gebhardt, K., Bender, R., Bower, G., et al. 2000, *Astroph.J.Lett.*, 539, L13, doi: [10.1086/312840](https://doi.org/10.1086/312840)
- Genzel, R., Eisenhauer, F., & Gillessen, S. 2024, *Astron. Astrophys. Rev.*, 32, 3, doi: [10.1007/s00159-024-00154-z](https://doi.org/10.1007/s00159-024-00154-z)
- Ghez, A. M., Salim, S., Hornstein, S. D., et al. 2005, *ApJ*, 620, 744, doi: [10.1086/427175](https://doi.org/10.1086/427175)
- Gilbert, O., Ruan, J. J., Eracleous, M., Haggard, D., & Runnoe, J. C. 2024. <https://arxiv.org/abs/2409.10486>
- Gillessen, S., Eisenhauer, F., Trippe, S., et al. 2009, *ApJ*, 692, 1075, doi: [10.1088/0004-637X/692/2/1075](https://doi.org/10.1088/0004-637X/692/2/1075)
- Giustini, M., Miniutti, G., & Saxton, R. D. 2020, *Astronomy&Astrophysics*, 636, L2, doi: [10.1051/0004-6361/202037610](https://doi.org/10.1051/0004-6361/202037610)
- Giustini, M., et al. 2024. <https://arxiv.org/abs/2409.01938>
- Götz, D., Paul, J., Basa, S., et al. 2009, in *American Institute of Physics Conference Series*, Vol. 1133, *Gamma-ray Burst: Sixth Huntsville Symposium*, ed. C. Meegan, C. Kouveliotou, & N. Gehrels (AIP), 25–30, doi: [10.1063/1.3155898](https://doi.org/10.1063/1.3155898)
- GRAVITY Collaboration, Abuter, R., Amorim, A., et al. 2018, *Astronomy&Astrophysics*, 615, L15, doi: [10.1051/0004-6361/201833718](https://doi.org/10.1051/0004-6361/201833718)
- Gravity Collaboration, Sturm, E., Dexter, J., et al. 2018, *Nature*, 563, 657, doi: [10.1038/s41586-018-0731-9](https://doi.org/10.1038/s41586-018-0731-9)
- Greene, J. E., Strader, J., & Ho, L. C. 2020, *ARA&A*, 58, 257, doi: [10.1146/annurev-astro-032620-021835](https://doi.org/10.1146/annurev-astro-032620-021835)
- Gültekin, K., Richstone, D. O., Gebhardt, K., et al. 2009, *ApJ*, 698, 198, doi: [10.1088/0004-637X/698/1/198](https://doi.org/10.1088/0004-637X/698/1/198)
- Guolo, M., Pasham, D. R., Zajaček, M., et al. 2024, *Nature Astronomy*, doi: [10.1038/s41550-023-02178-4](https://doi.org/10.1038/s41550-023-02178-4)
- Heckman, T. M., & Best, P. N. 2014, *ARA&A*, 52, 589, doi: [10.1146/annurev-astro-081913-035722](https://doi.org/10.1146/annurev-astro-081913-035722)
- Hernández-García, L., et al. 2025. <https://arxiv.org/abs/2504.07169>
- Ho, L. C., & Kim, M. 2014, *ApJ*, 789, 17, doi: [10.1088/0004-637X/789/1/17](https://doi.org/10.1088/0004-637X/789/1/17)
- Huang, Y., Xiao, J., Tao, L., et al. 2024, *Experimental Astronomy*, 58, 16, doi: [10.1007/s10686-024-09963-7](https://doi.org/10.1007/s10686-024-09963-7)

- Isi, M., Chatziioannou, K., & Farr, W. M. 2019, *PhRvL*, 123, 121101, doi: [10.1103/PhysRevLett.123.121101](https://doi.org/10.1103/PhysRevLett.123.121101)
- Ivezić, Ž., Kahn, S. M., Tyson, J. A., et al. 2019, *ApJ*, 873, 111, doi: [10.3847/1538-4357/ab042c](https://doi.org/10.3847/1538-4357/ab042c)
- Jiang, N., & Pan, Z. 2025, *Astroph.J.Lett.*, 983, L18, doi: [10.3847/2041-8213/adc456](https://doi.org/10.3847/2041-8213/adc456)
- Kaur, K., Rom, B., & Sari, R. 2024. <https://arxiv.org/abs/2406.07627>
- Kejriwal, S., Witzany, V., Zajacek, M., Pasham, D. R., & Chua, A. J. K. 2024, *Mon. Not. Roy. Astron. Soc.*, 532, 2143, doi: [10.1093/mnras/stae1599](https://doi.org/10.1093/mnras/stae1599)
- Kormendy, J., & Ho, L. C. 2013, *ARA&A*, 51, 511, doi: [10.1146/annurev-astro-082708-101811](https://doi.org/10.1146/annurev-astro-082708-101811)
- Kormendy, J., & Richstone, D. 1995, *ARA&A*, 33, 581, doi: [10.1146/annurev.aa.33.090195.003053](https://doi.org/10.1146/annurev.aa.33.090195.003053)
- Li, P., Yin, Q.-Q., Li, Z., et al. 2023, *Experimental Astronomy*, 55, 447, doi: [10.1007/s10686-022-09879-0](https://doi.org/10.1007/s10686-022-09879-0)
- Linial, I., & Metzger, B. D. 2023a, arXiv e-prints, arXiv:2303.16231, doi: [10.48550/arXiv.2303.16231](https://doi.org/10.48550/arXiv.2303.16231)
- . 2023b, arXiv e-prints, arXiv:2311.16231, doi: [10.48550/arXiv.2311.16231](https://doi.org/10.48550/arXiv.2311.16231)
- Linial, I., & Metzger, B. D. 2024. <https://arxiv.org/abs/2404.12421>
- Linial, I., & Quataert, E. 2023, doi: [10.1093/mnras/stad3470](https://doi.org/10.1093/mnras/stad3470)
- McConnell, N. J., & Ma, C.-P. 2013, *ApJ*, 764, 184, doi: [10.1088/0004-637X/764/2/184](https://doi.org/10.1088/0004-637X/764/2/184)
- Miniutti, G., Giustini, M., Arcodia, R., et al. 2023a, *Astronomy&Astrophysics*, 674, L1, doi: [10.1051/0004-6361/202346653](https://doi.org/10.1051/0004-6361/202346653)
- . 2023b, *Astronomy&Astrophysics*, 670, A93, doi: [10.1051/0004-6361/202244512](https://doi.org/10.1051/0004-6361/202244512)
- Miniutti, G., Saxton, R. D., Giustini, M., et al. 2019, *Nature*, 573, 381, doi: [10.1038/s41586-019-1556-x](https://doi.org/10.1038/s41586-019-1556-x)
- Miniutti, G., et al. 2024. <https://arxiv.org/abs/2411.13460>
- Nicholl, M., Pasham, D. R., Mummery, A., et al. 2024, Quasi-periodic X-ray eruptions years after a nearby tidal disruption event. <https://arxiv.org/abs/2409.02181>
- Pasham, D., Kejriwal, S., Coughlin, E., et al. 2024. <https://arxiv.org/abs/2411.00289>
- Pasham, D. R., Coughlin, E. R., Zajacek, M., et al. 2024, arXiv e-prints, arXiv:2402.09690. <https://arxiv.org/abs/2402.09690>
- Peterson, B. M. 2014, *SSRv*, 183, 253, doi: [10.1007/s11214-013-9987-4](https://doi.org/10.1007/s11214-013-9987-4)
- Peterson, B. M., Bentz, M. C., Desroches, L.-B., et al. 2005, *ApJ*, 632, 799, doi: [10.1086/444494](https://doi.org/10.1086/444494)
- Scheuer, P. A. G., & Feiler, R. 1996, *MNRAS*, 282, 291, doi: [10.1093/mnras/282.1.291](https://doi.org/10.1093/mnras/282.1.291)
- Schmidt, W. 2002, *Classical and Quantum Gravity*, 19, 2743, doi: [10.1088/0264-9381/19/10/314](https://doi.org/10.1088/0264-9381/19/10/314)
- Schödel, R., Ott, T., Genzel, R., et al. 2002, *Nature*, 419, 694, doi: [10.1038/nature01121](https://doi.org/10.1038/nature01121)
- Shapiro, I. I. 1964, *Phys. Rev. Lett.*, 13, 789, doi: [10.1103/PhysRevLett.13.789](https://doi.org/10.1103/PhysRevLett.13.789)
- Shen, Y. 2013, *Bulletin of the Astronomical Society of India*, 41, 61, doi: [10.48550/arXiv.1302.2643](https://doi.org/10.48550/arXiv.1302.2643)
- Sun, L., Shu, X., & Wang, T. 2013, *ApJ*, 768, 167, doi: [10.1088/0004-637X/768/2/167](https://doi.org/10.1088/0004-637X/768/2/167)
- Tagawa, H., & Haiman, Z. 2023, *Mon. Not. Roy. Astron. Soc.*, 526, 69, doi: [10.1093/mnras/stad2616](https://doi.org/10.1093/mnras/stad2616)
- Tremaine, S., Gebhardt, K., Bender, R., et al. 2002, *ApJ*, 574, 740, doi: [10.1086/341002](https://doi.org/10.1086/341002)
- van de Meent, M. 2020, *Class. Quant. Grav.*, 37, 145007, doi: [10.1088/1361-6382/ab79d5](https://doi.org/10.1088/1361-6382/ab79d5)
- Vurm, I., Linial, I., & Metzger, B. D. 2024. <https://arxiv.org/abs/2410.05166>
- Waisberg, I., Dexter, J., Gillessen, S., et al. 2018, *Monthly Notices of the Royal Astronomical Society*, 476, 3600, doi: [10.1093/mnras/sty476](https://doi.org/10.1093/mnras/sty476)
- Wang, T., Liu, G., Cai, Z., et al. 2023a, *Science China Physics, Mechanics, and Astronomy*, 66, 109512, doi: [10.1007/s11433-023-2197-5](https://doi.org/10.1007/s11433-023-2197-5)
- Wang, Y., Zhu, Z., & Lin, D. N. C. 2023b, arXiv e-prints, arXiv:2308.09129, doi: [10.48550/arXiv.2308.09129](https://doi.org/10.48550/arXiv.2308.09129)
- Wevers, T., Pasham, D. R., Jalan, P., Rakshit, S., & Arcodia, R. 2022, *Astronomy&Astrophysics*, 659, L2, doi: [10.1051/0004-6361/202243143](https://doi.org/10.1051/0004-6361/202243143)
- Wevers, T., French, K. D., Zabludoff, A. I., et al. 2024, *Astroph.J.Lett.*, 970, L23, doi: [10.3847/2041-8213/ad5f1b](https://doi.org/10.3847/2041-8213/ad5f1b)
- Williams, M. J. 2021, *nessai: Nested Sampling with Artificial Intelligence*, latest, Zenodo, doi: [10.5281/zenodo.4550693](https://doi.org/10.5281/zenodo.4550693)
- Woo, J.-H., Cho, H., Gallo, E., et al. 2019, *Nature Astronomy*, 3, 755, doi: [10.1038/s41550-019-0790-3](https://doi.org/10.1038/s41550-019-0790-3)
- Xian, J., Zhang, F., Dou, L., He, J., & Shu, X. 2021, *Astroph.J.Lett.*, 921, L32, doi: [10.3847/2041-8213/ac31aa](https://doi.org/10.3847/2041-8213/ac31aa)
- Yao, P. Z., Quataert, E., Jiang, Y.-F., Lu, W., & White, C. J. 2024. <https://arxiv.org/abs/2407.14578>
- Zanazzi, J. J., & Lai, D. 2019, *Mon. Not. Roy. Astron. Soc.*, 487, 4965, doi: [10.1093/mnras/stz1610](https://doi.org/10.1093/mnras/stz1610)
- Zhang, F., Lu, Y., & Yu, Q. 2015, *Astrophys. J.*, 809, 127, doi: [10.1088/0004-637X/809/2/127](https://doi.org/10.1088/0004-637X/809/2/127)
- Zhou, C., Huang, L., Guo, K., Li, Y.-P., & Pan, Z. 2024, *PhRvD*, 109, 103031, doi: [10.1103/PhysRevD.109.103031](https://doi.org/10.1103/PhysRevD.109.103031)
- Zhou, C., Zeng, Y., & Pan, Z. 2024a. <https://arxiv.org/abs/2411.18046>
- Zhou, C., Zhong, B., Zeng, Y., Huang, L., & Pan, Z. 2024b, *Phys. Rev. D*, 110, 083019, doi: [10.1103/PhysRevD.110.083019](https://doi.org/10.1103/PhysRevD.110.083019)